

Journal of Materials Chemistry A

Accepted Manuscript



This is an *Accepted Manuscript*, which has been through the Royal Society of Chemistry peer review process and has been accepted for publication.

Accepted Manuscripts are published online shortly after acceptance, before technical editing, formatting and proof reading. Using this free service, authors can make their results available to the community, in citable form, before we publish the edited article. We will replace this *Accepted Manuscript* with the edited and formatted *Advance Article* as soon as it is available.

You can find more information about *Accepted Manuscripts* in the [Information for Authors](#).

Please note that technical editing may introduce minor changes to the text and/or graphics, which may alter content. The journal's standard [Terms & Conditions](#) and the [Ethical guidelines](#) still apply. In no event shall the Royal Society of Chemistry be held responsible for any errors or omissions in this *Accepted Manuscript* or any consequences arising from the use of any information it contains.

Room-temperature CuAlO₂ hole interfacial layer for efficient and stable planar perovskite solar cells

Cite this: DOI: 10.1039/x0xx00000x

Femi Igbari, Meng Li, Yun Hu, Zhao-Kui Wang* and Liang-Sheng Liao*

Received 00th January 2012,
Accepted 00th January 2012

DOI: 10.1039/x0xx00000x

www.rsc.org/

The fabrication and device parameters of inverted planar heterojunction (PHJ) organic-inorganic lead mixed-halide (CH₃NH₃PbI_{3-x}Cl_x) perovskite based solar cells (PSCs) using a:CuAlO₂ as hole selective buffer layer between ITO electrode and PEDOT:PSS was demonstrated. The thin films of a:CuAlO₂ were derived from a pre-fabricated polycrystalline CuAlO₂ ceramic target via direct current (d.c.) magnetron sputtering technique. One-step spin coating method was used to prepare the perovskite layer. A short circuit current density (J_{sc}) of 21.98 mA/cm², an open circuit voltage (V_{oc}) of 0.88 V, a fill factor (FF) of 0.75 and a power conversion efficiency (PCE) of 14.52 % were achieved for the optimized device. These improved device parameters were also accompanied with improved stability as a result of sandwiching the ambient stable a:CuAlO₂ layer with decent conductivity between the ITO and the PEDOT:PSS layers. The versatility of this material application was also demonstrated as similar improvement in device performance and stability was observed by using the prepared a:CuAlO₂ in another perovskite solar cell system based on CH₃NH₃PbI₃ prepared by two-step spin-coating method.

Introduction

Organometallic halide provskites have shown great promises as light absorber layers in perovskite based solar cells.¹⁻⁶ This is due to their possession of interesting properties such as high absorption coefficient, direct band gap, excellent charge transport properties and long exciton diffusion length.⁷⁻¹¹ This unique properties have led to the rapid improvement in device performance within a short time with the best PCE currently above 20 %.¹²

The two major device architectures commonly reported for perovskite based solar cells are: the planar heterojunction (PHJ)^{13,14} and the meso structure.^{15,16} However, due to the limitations such as high temperature requirements for the formation of layers of metal oxide scaffold and the pore filling problems,¹⁷⁻²⁰ PHJ which has a simple structure in which the perovskite layer is sandwiched between a hole and an electron conductor stands out. The most widely used hole transport layer (HTL) in the PHJ device is poly(3,4-ethylenedioxythiophene):poly(styrenesulfonate) (PEDOT:PSS)²¹⁻²⁷ which is acidic in nature.^{28,29} This acidic property of PEDOT:PSS potends great long-term danger to the underlying ITO as it could be eroded after a while leading to a poorly stable device. Other materials such as nickel oxide (NiO),^{28,30-32} poly-(*N*-9'-hepta decanyl-2,7-cabazole-*alt*-5,5-(4',7'-di(thien-2-yl)-2',1',3'-benzothiadiazole)) (PCDTBT),^{33,34} lead sulphide (PbS),^{35,36} graphene oxide (GO)^{37,38} and germanium dioxide (GeO₂)²⁹ have been demonstrated as alternative hole transporting materials and in some cases, possible replacements for the acidic PEDOT:PSS. Their PCEs are however usually lower than those reported for PEDOT:PSS based devices.

Another factor which is pivotal to the actual practical application and commercialization of perovskite based solar cells but has not

been given adequate attention is the device stability. However few reports exist on the combination of advantages of MoO₃ and PEDOT:PSS as a composite and bilayer HTL. MoO₃ has been paid great attention for its high transmittance, nontoxicity, and high work function.³⁹⁻⁴⁴ This combination has been found to promote the performance and stability of solar cells.⁴⁵⁻⁴⁸ Bulk heterojunction polymer solar cells have been fabricated by inserting a solution-processed PEDOT/PSS anode buffer layer doped with solution processed metal oxides.^{45,46} However, to avoid the direct contact between PEDOT:PSS and ITO which still occurs in such a configuration, a facile method was developed to fabricate a solution processed e-MoO₃/PEDOT:PSS bilayer HTL for application in polymer solar cells.⁴⁷ Furthermore, solution processed MoO₃/PEDOT:PSS bilayer has been used as the HTL in inverted CH₃NH₃PbI₃ PHJ perovskite solar cells.⁴⁸ This bilayer system improves the efficiency and stability of the solar cells by decreasing series resistance, increasing the hole extraction efficiency and restraining erosion of ITO by PEDOT:PSS.

P-type CuAlO₂ has been reported to possess decent optical transparency, chemical and thermal stability and can be prepared from cheap, easily accessible and non-toxic elements.^{49,50} Its conductivity could also be as high as 1 S/cm.⁵¹ The application of CuAlO₂ bulk or film in perovskite solar cells is so far yet to be reported. This may be due to the high temperature needed for the preparation of its pure polycrystalline delafossite phase. However, Ahmed et al,⁵² Nattestad *et al.*⁵³ and bandara *et al.*⁵⁴ have reported the application of CuAlO₂ nanoparticles has HTL in dye sensitized solar cells (DSSCs) in which the device performance was explained to be a function of the nanoparticle size distribution and morphology. The preparation and application of amorphous CuAlO₂ (a:CuAlO₂) which does not require high temperature processing has been reported. Li *et al.*⁵⁵ prepared a:CuAlO₂ thin films via radio

frequency (r.f.) magnetron sputtering from sintered targets composed of $\text{Al}(\text{OH})_3$ and Cu_2O precursors. They reported a direct band gap of 3.86 eV for the as-deposited film. Bu⁵⁶ also grew amorphous p-type CuAlO_2 thin films on n-type crystalline ZnO nanowires to form a heterojunction with photovoltaic properties. It is important to note that the magnetron sputtering technique is capable of generating a wide area, continuous and compact film which is without voids through which a direct contact between the acidic PEDOT:PSS and the ITO may occur. It is also a physical deposition method in which no solvent is required for sample deposition. It therefore does not create chances of wet chemical reactions between the a: CuAlO_2 and ITO.

Here we demonstrate the application of an a: CuAlO_2 as a hole selective interfacial layer between ITO and PEDOT:PSS in the fabrication of $\text{CH}_3\text{NH}_3\text{PbI}_{3-x}\text{Cl}_x$ perovskite based solar cell with an inverted device architecture. The a: CuAlO_2 layer was deposited by the d.c. magnetron sputtering technique. The a: CuAlO_2 due to its stability and decent conductivity served two purposes of enhancing the extraction of photogenerated charges from the active $\text{CH}_3\text{NH}_3\text{PbI}_{3-x}\text{Cl}_x$ provskite layer into the ITO and completely preventing the direct contact between the acidic PEDOT:PSS and ITO. These combined advantages ensure the improvement in the device parameters of the PSCs fabricated with a: CuAlO_2 compared to the reference PSCs which are without a: CuAlO_2 . The optimized device having 15 nm a: CuAlO_2 layer shows improved stability by retaining about 80 % of its initial PCE while the reference device only retained 35 % of its PCE after storage in ambient for 240 hours.

Results and discussion

The CuAlO_2 polycrystalline ceramic sputter target and the resulting a: CuAlO_2 thin films prepared via d.c. magnetron sputtering technique were characterized using XRD. Fig. S1(a) displays the XRD patterns of a representative a: CuAlO_2 and the pure delafossite crystal phase of the CuAlO_2 ceramic target. All the peaks which can be attributed to the precursor materials as well as other intermediate species in the crystal phase transition are not found in the CuAlO_2 XRD pattern. This indicates that pure CuAlO_2 powder and ceramic target can be achieved using our technique (Experimental section, Supporting information). The need to maintain a Cu:Al:O ratio of 1:1:2 in the a: CuAlO_2 films necessitated the use of a delafossite CuAlO_2 ceramic target. A typical EDX spectrum confirming this atomic ratio for a: CuAlO_2 is presented in Fig. S1(b). The XRD pattern of the representative a: CuAlO_2 thin film shows no obvious diffraction peaks. This confirms the amorphous nature of the film. The formation of such amorphous materials from a polycrystalline target is attributed to the introduction of a measure of structural disorder as the material is being deposited in vapour form onto the substrate.

The conductivity of the prepared a: CuAlO_2 film which is expected to vary as a function of film thickness was studied and was compared with the conductivity of PEDOT:PSS film (40 nm). To achieve this, Hall effect measurements were carried out on the samples using the van der Pauw method. Table 1 shows the

parameters obtained for the conductivities of PEDOT:PSS and the various thicknesses of a: CuAlO_2 films. These results are within the range of values previously reported by other authors.^{27,54,57-60} The movement of charge carriers becomes easier if the packing density and consequently the conductivity of the films increase. Hence we speculate that increase in packing density as a result of increased film thickness makes substantial contribution to the electrical conductivity. However, activation energy also plays a vital role in thin film conductivity. Therefore, to further understand the origin of this phenomenon, we conducted a temperature dependent conductivity test on the thin films within the temperature range of 273 K and 300 K. The variation of logarithmic conductivity as a function of inverse of temperature (Arrhenius plot) is shown in Fig. S2. This variation can be expressed by the equation $\sigma = \sigma_0 \exp\left(-\frac{E_A}{kT}\right)$ where σ_0 is conductivity at infinite temperature, E_A the thermal activation energy and k is the Boltzmann's constant. Activation energies of 0.16, 0.03, 0.02, 0.01 and 0.005 eV were therefore extracted for PEDOT:PSS (40 nm), 5, 10, 15 and 20 nm a: CuAlO_2 respectively. It was found that the activation energy decreases continuously while the electrical conductivity progressively increases. Such relationship between E_A and σ has previously been reported.^{61,62} We therefore conclude that the increase in the conductivity of the a: CuAlO_2 films is due to the decrease in activation energy as the film thickness increases. From Table 1, it can also be seen that the obtained conductivity values for prepared a: CuAlO_2 are higher than that of the PEDOT:PSS film. It is known that inorganic materials show better electronic behaviour than their organic counterparts. As explained later, the insertion of a stable a: CuAlO_2 with decent conductivity and suitable energy level alignment between the ITO electrode and PEDOT:PSS can lead to a reduction in series resistance (R_s) by eliminating contact resistance created as a result of the harsh acidic effect of PEDOT:PSS on ITO. This leads to enhanced charge extraction.

In addition to the electronic properties, the workfunction (WF) of the a: CuAlO_2 was also seen as a function of film thickness. From the UPS spectra of PEDOT:PSS and the various thicknesses of a: CuAlO_2 obtained by using Helium lamp emitting at 21.2 eV as presented in Fig. 1, it can be seen that the secondary cut-off regions for films with 5, 10, 15 and 20 nm thicknesses are 16.2, 16.1, 16.0 and 15.9 eV respectively. Thus, the calculated WFs for these films are 5.0, 5.1, 5.2 and 5.3 eV respectively as shown in Table 1. It was observed from this measurement that the workfunction of the 15 nm a: CuAlO_2 film matches with that of PEDOT:PSS.

AFM images in Fig. S3(a, c, e and g) show a reduction in the root mean square (rms) roughness of the films from 1.24 nm to 0.63 nm as the thickness increased from 5 nm to 20 nm. The variation in WF is therefore due to changes in the surface roughness as the film thickness increases. WF, a fundamental electronic property of materials is extremely sensitive to surface conditions.⁶³ Some existing results⁶⁴⁻⁶⁷ show that the larger the surface roughness is, the smaller WF becomes.

Metal-oxide work functions can also be tuned over a continual range by changing the concentration of defects. Removing oxygen

tends to decrease the work function, whereas adding oxygen tends to increase the work function.^{68,69} Removal of oxygen through the formation of O vacancies results in cation centers with reduced

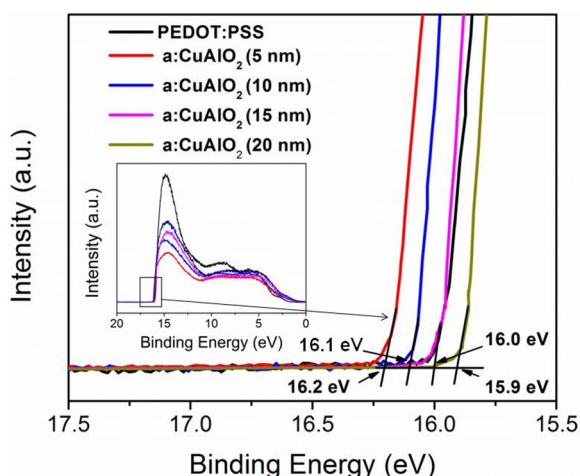


Fig. 1. UPS spectra revealing the secondary cut-off regions for PEDOT:PSS (40 nm) and 5, 10, 15 and 20 nm a:CuAlO₂ films.

Table 1. Conductivity values for PEDOT:PSS and a:CuAlO₂ films as obtained from Hall effect measurements, their workfunctions calculated from UPS results and their activation energies extracted from Arrhenius plots.

Samples	σ (S/cm)	WF (eV)	E_A (eV)
PEDOT:PSS (40 nm)	0.01	5.2	0.16
a:CuAlO ₂ (5 nm)	0.09	5.0	0.03
a:CuAlO ₂ (10 nm)	0.11	5.1	0.02
a:CuAlO ₂ (15 nm)	0.13	5.2	0.01
a:CuAlO ₂ (20 nm)	0.15	5.3	0.005

oxidation states. As the concentration of reduced cations increases, an oxide's electronegativity and subsequently its work function decrease. The formation of O vacancies is as a result of interfacial redox interactions taking place at the electrode/metal oxide (in this case, ITO/a:CuAlO₂) interface and it is induced by the difference in oxidation potentials (E_{pa}) of the electrode and metal oxide. To confirm this we carried out cyclic voltammetry on separate films of ITO and a:CuAlO₂ used in this work. A three-electrode scheme was used. ITO and sputtered a:CuAlO₂ thin films were used in turn as the working electrode, Ag/AgCl wire in a 3.5 M KCl aqueous solution as reference electrode and Pt wire as counter-electrode. The electrolyte used was 0.1 M aqueous KCl. Fig. S5(a) shows the voltammograms obtained for both films. It can be seen that the magnitude of the E_{pa} of ITO (1.34 V) is greater than that of a:CuAlO₂ (1.12 V). This suggests a removal of oxygen anions by the ITO electrode from the metal oxide buffer layer. This induces oxygen vacancies in the a:CuAlO₂ buffer layer. Fig. S5(b) shows the O 1s core level spectrum obtained from XPS analysis conducted on the ITO/a:CuAlO₂ film. From the XPS pattern, it can be seen that the concentration of created defect is a function of film

thickness as a reduction in the intensity of oxygen anions is observed as the a:CuAlO₂ film thickness decreases. The induced oxygen vacancies are defects which create cation centers with reduced oxidation states which are responsible for lowering the work function.

Fig. S3(b, d, f and h) show the plan view SEM images of the a:CuAlO₂ films on ITO. It can also be seen from these images that the surface roughness decreased as the film thickness increased and that a complete coverage of the ITO layer is achieved regardless of the thickness of the a:CuAlO₂ film. This is due to the effectiveness of the sputter deposition technique. This complete coverage is important as it prevents the creation of voids through which a direct contact can be created between the PEDOT:PSS layer and the ITO layer. Fig. S4(a-e) shows the AFM images of the pristine PEDOT:PSS film and PEDOT:PSS films deposited on the 5, 10, 15 and 20 nm a:CuAlO₂ films. The rms roughness of the PEDOT:PSS films are observed to be 1.23, 1.25, 1.24, 1.23 and 1.22 nm respectively showing that they are all comparable. This similarity in surface roughness shows that the underlying a:CuAlO₂ does not affect the surface properties of the PEDOT:PSS layer. This could be as a result of the significant difference between the thickness of the PEDOT:PSS layer and those of the a:CuAlO₂ underlying films and the similarities in the thicknesses of the pristine PEDOT:PSS film and PEDOT:PSS films with a:CuAlO₂ underlayers as they were all deposited by spin-coating at 4500 rpm for 40 sec and annealed at 140 °C for 20 min to yield a thickness of 40 nm (as analysed by AFM).

The optical properties of the ITO/a:CuAlO₂ layers which is crucial to the magnitude of absorbed incident photon by the absorber layer was studied and was compared to that of the neat ITO. From Fig. 2,

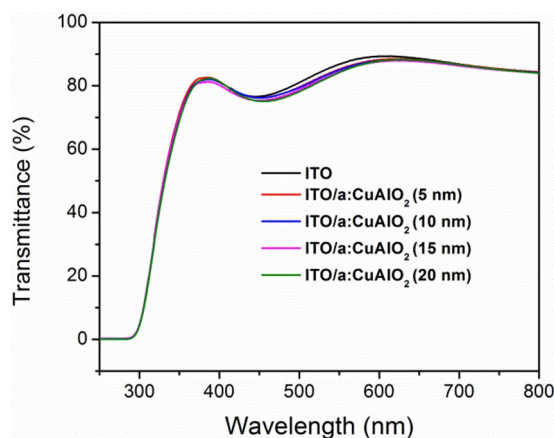


Fig. 2. Transmittance spectra of the neat ITO and ITO/(5, 10, 15 and 20 nm) a:CuAlO₂ films.

it can be seen that due to the high transparency of the a:CuAlO₂ thin films, the ITO/a:CuAlO₂ layers exhibit remarkable transparency of up to 80 % comparable to that of the neat ITO. This shows that the incorporation of thin films of a:CuAlO₂ does not impair the optical property required for an optimum operation of the solar cell.

XRD analysis of the $\text{CH}_3\text{NH}_3\text{PbI}_{3-x}\text{Cl}_x$ grown on the a:CuAlO₂/PEDOT:PSS bilayer and on the pristine PEDOT:PSS was conducted to confirm the effective formation of the perovskite layer with or without the incorporation of the a:CuAlO₂. Fig. 3 shows the XRD patterns. The peaks denoted by (110), (220), (310) and (312) which are attributed to pure $\text{CH}_3\text{NH}_3\text{PbI}_{3-x}\text{Cl}_x$ perovskite phase show that a complete reaction took place between the $\text{CH}_3\text{NH}_3\text{I}$ and PbCl_2 as the peaks which could be assigned to unreacted precursors or reaction intermediates do not exist in the pattern.

The similarities in peak patterns of the various bilayer configurations and the pristine PEDOT:PSS confirms the effective formation of the perovskite absorber layer irrespective of the underlayers. Fig. 4 shows the plan view SEM images of a typical $\text{CH}_3\text{NH}_3\text{PbI}_{3-x}\text{Cl}_x$ film on a:CuAlO₂/PEDOT:PSS layer with the various thicknesses of a:CuAlO₂ and $\text{CH}_3\text{NH}_3\text{PbI}_{3-x}\text{Cl}_x$ on pristine PEDOT:PSS. Both films exhibit a homogeneous, compact and continuous morphology. Such morphology ensures high charge mobility and a low electron-hole recombination in perovskite based solar cells.

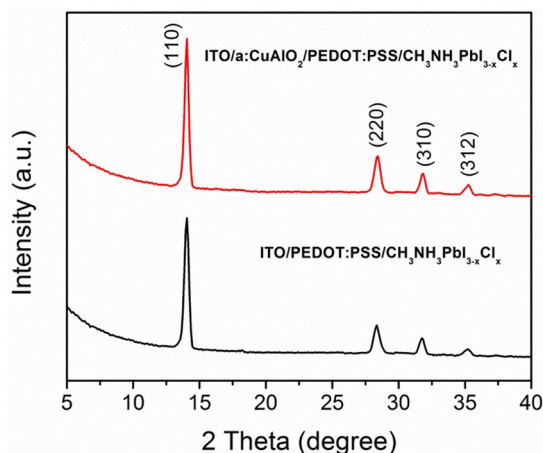


Fig. 3. Typical XRD pattern for $\text{CH}_3\text{NH}_3\text{PbI}_{3-x}\text{Cl}_x$ with various configurations of a:CuAlO₂/PEDOT:PSS underlayer (red line) and XRD pattern for $\text{CH}_3\text{NH}_3\text{PbI}_{3-x}\text{Cl}_x$ on pristine PEDOT:PSS layer (black line).

Photoluminescence (PL) quenching efficiency of the perovskite emission was then conducted to study its compatibility with our a:CuAlO₂ thin film. Structures of ITO/ $\text{CH}_3\text{NH}_3\text{PbI}_{3-x}\text{Cl}_x$, ITO/PEDOT:PSS/ $\text{CH}_3\text{NH}_3\text{PbI}_{3-x}\text{Cl}_x$ and ITO/a:CuAlO₂/PEDOT:PSS/ $\text{CH}_3\text{NH}_3\text{PbI}_{3-x}\text{Cl}_x$ with the various a:CuAlO₂ thicknesses were compared. Excitation wavelength of 530 nm as confirmed from the absorbance spectra obtained from UV/Vis analysis (Fig. S6) was used for the PL measurements. Fig. 5 shows the PL emission spectra with peaks of the ITO/ $\text{CH}_3\text{NH}_3\text{PbI}_{3-x}\text{Cl}_x$ structure found around 770 nm. The sharp reduction in the PL intensities indicated that the PL quenching efficiencies increased significantly as PEDOT:PSS and a:CuAlO₂ layers are being added to the structures with the structures having a:CuAlO₂ showing comparable efficiency with the structures having pristine PEDOT:PSS. This shows that the addition of a:CuAlO₂ does not impair the PL quenching efficiency of PEDOT:PSS and can

enhance the extraction of photogenerated charge due to its increased conductivity.

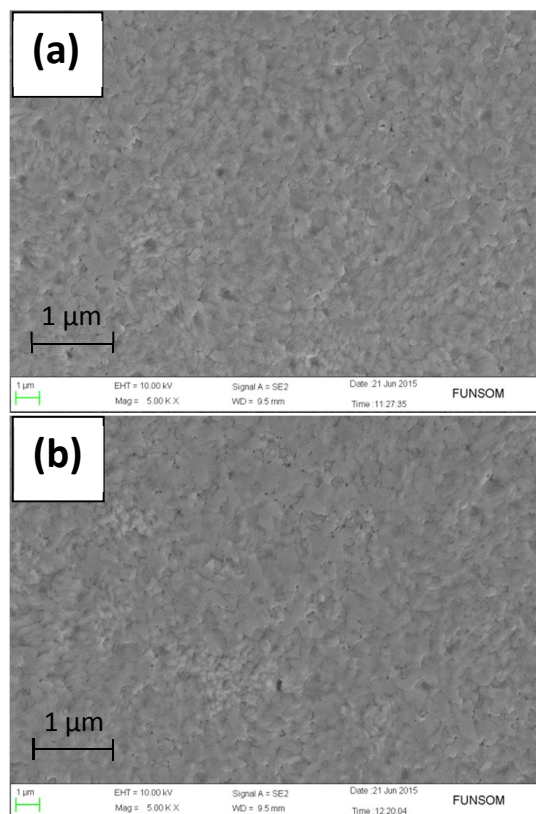


Fig. 4. (a) A typical plan view SEM image of $\text{CH}_3\text{NH}_3\text{PbI}_{3-x}\text{Cl}_x$ on a:CuAlO₂/PEDOT:PSS layer, (b) plan view SEM image of $\text{CH}_3\text{NH}_3\text{PbI}_{3-x}\text{Cl}_x$ on pristine PEDOT:PSS.

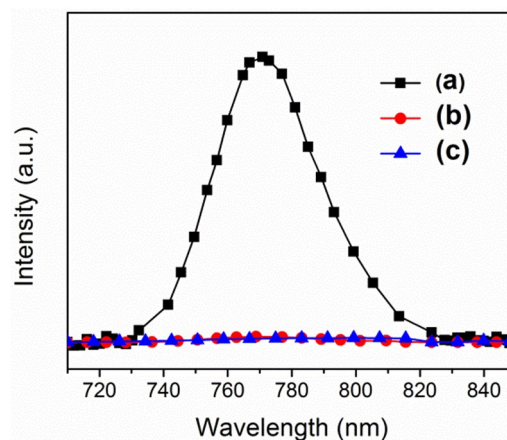


Fig. 5. PL spectra of $\text{CH}_3\text{NH}_3\text{PbI}_{3-x}\text{Cl}_x$ on top of (a) ITO, (b) PEDOT:PSS and (c) a:CuAlO₂/PEDOT:PSS measured at an excitation wavelength of 530 nm.

Based on these properties, $\text{CH}_3\text{NH}_3\text{PbI}_{3-x}\text{Cl}_x$ perovskite based solar cells were fabricated using the a:CuAlO₂/PEDOT:PSS bilayer hole conductor and were compared with a reference device which was fabricated without a:CuAlO₂. PEDOT:PSS layer with a thickness of

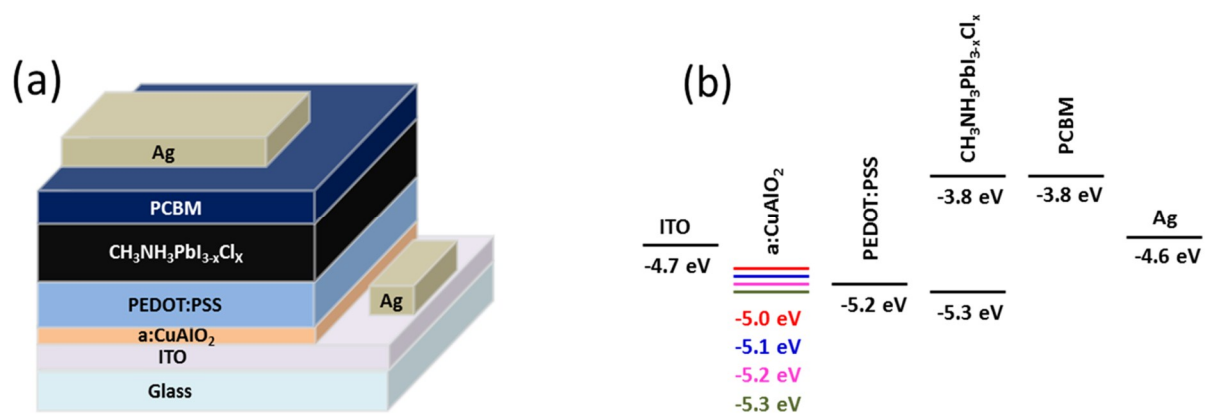


Fig. 6. (a) Device structure of the fabricated device with a:CuAlO₂ buffer layer and (b) energy level diagram of the device components along with the various thicknesses of a:CuAlO₂: red line (5 nm), blue line (10 nm), pink line (15 nm) and olive line (20 nm).

40 nm was used in devices fabricated with and without a:CuAlO₂. Six devices were fabricated in each case and the obtained device parameters were averaged. Fig. 6(a) shows the device structure of the fabricated device and Fig 6(b) is the energy level diagram of the device components as obtained from literature along with the various thicknesses of a:CuAlO₂ as calculated from our UPS measurements.

In Fig. 7(a), the J - V curves of the CH₃NH₃PbI_{3-x}Cl_x perovskite based solar cells with different a:CuAlO₂ film thicknesses and the reference device are presented. The detailed device parameters extracted from the curves are presented in Table 2. From this table, it is seen that the reference device possesses a J_{sc} of 18.79 mA/cm², a V_{oc} of 0.88 V, an FF of 0.67 and a PCE of 11.10 %. Similarities were observed in the V_{oc} of both the reference device and devices with various thicknesses of a:CuAlO₂. This is as a result of the similarities in their PEDOT:PSS/CH₃NH₃PbI_{3-x}Cl_x interfaces, the CH₃NH₃PbI_{3-x}Cl_x bulk and the CH₃NH₃PbI_{3-x}Cl_x/PCBM interfaces. An improvement was however observed in the J_{sc} , FF and consequently the PCE of the devices with a:CuAlO₂.

This improvement stems from the enhanced charge extraction and reduced charge recombination due to the incorporation of an

a:CuAlO₂ with increased conductivities and suitable workfunctions as explained later. A slight drop in the device parameters was observed as the a:CuAlO₂ film thickness was increased to 20 nm. From this obtained parameters it is seen that the optimized device is the one with 15 nm a:CuAlO₂ which exhibits a J_{sc} of 21.98 mA/cm², a V_{oc} of 0.88 V, an FF of 0.75 and a PCE of 14.52 %. Compared with the reference device, the PCE of the optimized device is increased by more than 30% as a result of about 17 % and 12 % improvements in its J_{sc} and FF respectively. The EQE data obtained from the devices are shown in Fig.7(b). It can be seen that the curves obtained confirm the J - V curve results with the optimized device exhibiting a much higher photon-to-electron conversion efficiency compared to the pristine PEDOT:PSS-based device. A shape similarity is also observed in the EQE response of the devices with and without a:CuAlO₂ and this supports the information obtained from the PL spectra that excitons are effectively quenched in devices with and without a:CuAlO₂. These results confirm that the addition of an a:CuAlO₂ buffer layer between ITO and PEDOT:PSS is an effective way to improve device performance by increasing electrical conductivity, charge extraction efficiency and restraining charge recombination.

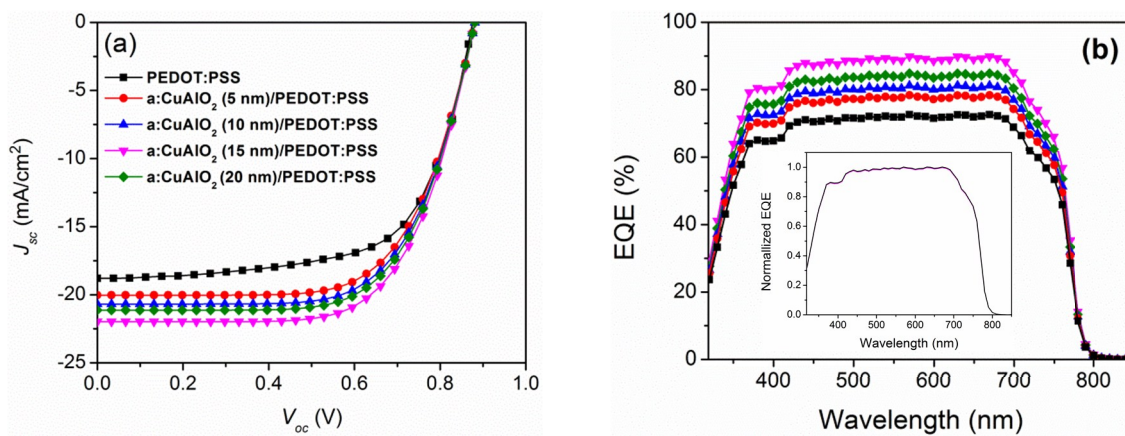


Fig. 7. (a) J - V characteristics and (b) EQE spectra of the devices with different configurations of a:CuAlO₂/PEDOT:PSS and pristine PEDOT:PSS hole conductors.

Table 2. Photovoltaic parameters of the reference device and the device with different a:CuAlO₂/PEDOT:PSS configurations.

	J_{sc} (mA/cm ²)	V_{oc} (V)	FF	η (%)	R_s (Ω cm ⁻²)	R_p (k Ω cm ⁻²)
PEDOT:PSS (40 nm)	18.79 ± 0.56	0.88 ± 0.01	0.67 ± 0.02	11.10 ± 0.78	5.97	1.48
a:CuAlO ₂ (5 nm)/PEDOT:PSS	20.03 ± 0.55	0.88 ± 0.02	0.71 ± 0.01	12.54 ± 0.80	4.86	1.87
a:CuAlO ₂ (10 nm)/PEDOT:PSS	20.68 ± 0.54	0.88 ± 0.02	0.73 ± 0.02	13.31 ± 1.01	4.32	1.52
a:CuAlO ₂ (15 nm)/PEDOT:PSS	21.98 ± 0.34	0.88 ± 0.01	0.75 ± 0.01	14.52 ± 0.58	3.23	1.91
a:CuAlO ₂ (20 nm)/PEDOT:PSS	21.13 ± 0.49	0.88 ± 0.01	0.74 ± 0.01	13.77 ± 0.66	3.67	1.64

The origin of this improved device performance can be traced to the increased conductivity of the added a:CuAlO₂ layer and its formation of adequate energy level alignments with the PEDOT:PSS layer. Table 1 shows a comparison between the conductivities of the a:CuAlO₂ layers and the PEDOT:PSS. Since the photoluminescence quenching efficiency of PEDOT:PSS (Fig. 5) is not impaired by the addition of a:CuAlO₂ layer, the increased conductivity of a:CuAlO₂ ensures enhanced extraction and transport of the photogenerated charges through the hole conducting bilayer into the electrode. This enhanced charge extraction ensures efficient charge separation and restrained recombination. As a result, there exists a reduction in the series resistances (R_s) of the devices with a:CuAlO₂ while their shunt resistances (R_p) are comparable to that of the reference device as shown in Table 2.

In addition, the WF of the various thicknesses of the a:CuAlO₂ also affects the ease with which charges are extracted from the active layer into the electrode. The energy level diagram as obtained from the UPS analysis in Fig. 1 is presented in Fig. 6(b). It can be seen that the workfunction of the 15 nm a:CuAlO₂ aligns perfectly with that of the PEDOT:PSS film. This contributes to the effective charge extraction as there exists no energy barrier at the interface. It also explains why this device presents better performance than the other devices with a:CuAlO₂ as they exhibit considerable energy barriers with the PEDOT:PSS. Despite this energy level barriers, it is observed that they still possess improved device parameters compared to the reference device. This is because the energy barriers created are suitable enough to form cascade energy alignments⁷⁰⁻⁷² with the PEDOT:PSS layer and the ITO electrode. This is energetically favourable for charge transfer as it blocks the back flow of the extracted photogenerated charges and improves their injection into the electrode. Although this cascade energy alignment is not seen in the 20 nm a:CuAlO₂ as it possesses a higher WF of 5.3 eV, enhanced photogenerated charge (hole) extraction can be due to the Ohmic contact created at the ITO/a:CuAlO₂ interface as a result of its increased conductivity. This lack of energy level alignment however creates a relative increase in R_s (Table 2) and explains why there exists a slight reduction in device

parameters such as J_{sc} and FF of the device with 20 nm a:CuAlO₂ compared to the optimized device.

To obtain a deeper insight of the role of the a:CuAlO₂ buffer layer in the performance of perovskite solar cells, electrical impedance spectroscopy (EIS) was used to study the interface charge transport in the perovskite solar cell. It was observed that the a:CuAlO₂ hole selective buffer layer can forcefully reduce the charge transfer resistance between the ITO and the PEDOT:PSS film, as shown in Fig. 8(a). The Nyquist plots of the devices were measured at 0.88 V in dark condition and the equivalent circuit model for the perovskite solar cells is shown in the inset of Fig. 8(a). The fitted equivalent circuit model is composed of series resistance (R_s) and charge transfer resistance (R_{CT}) which forms a parallel circuit with capacitor C_{CT} . The parameters of the equivalent circuit with and without a:CuAlO₂ are summarized in Table S1. It is clear that the device without a:CuAlO₂ exhibits the largest R_{CT} of 384.03 Ω indicating the poorest charge transport properties as witnessed by the lowest J_{sc} (Table 2). The R_{CT} is found to be notably decreased to 221.77 Ω for the optimized perovskite solar cells based on the 15 nm a:CuAlO₂ suggesting that the contact resistance existing between the PEDOT:PSS layer and ITO electrode (which may be due to the harsh acidic effect of PEDOT:PSS on ITO) disappears with the addition of a:CuAlO₂. Since contact resistance contributes to the R_s in devices, we therefore conclude that the reduction in the R_s in devices with a:CuAlO₂ results from the disappearance of contact resistance. These reductions in R_s and R_{CT} imply more efficient extraction/transport of the holes resulting in increased J_{sc} and FF for the solar cells.

The current density–voltage characteristics of these devices were also measured under dark conditions. From Fig. 8(b), It can be found that the dark currents of the a:CuAlO₂/PEDOT:PSS based devices are higher than those of the reference device. The highest dark current is found in the device with a:CuAlO₂(15 nm)/PEDOT:PSS which corresponds to the highest PCE among the devices. These increased dark currents indicate a reduction in series resistance (R_s)⁴⁸ which leads an improvement in the photogenerated charge extraction efficiency as explained earlier.

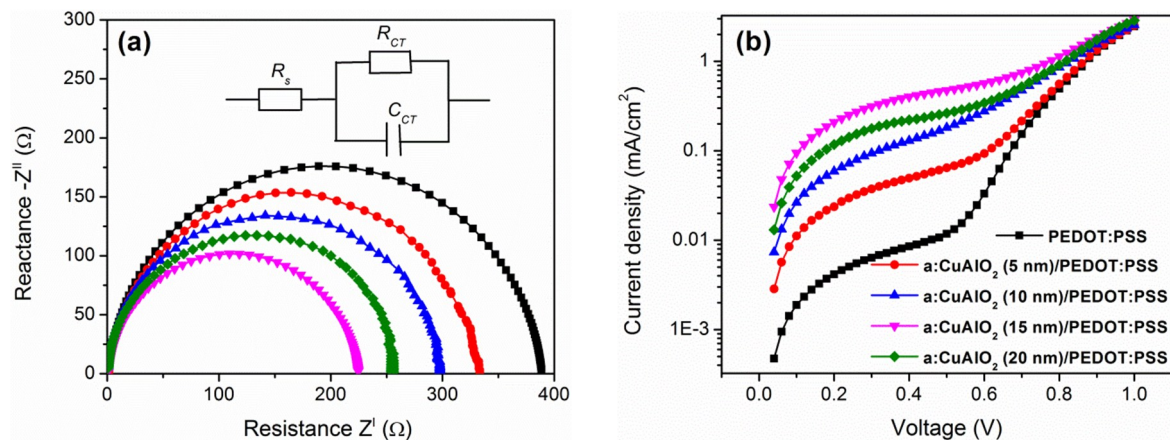


Fig. 8. (a) Nyquist plots measured at the V_{oc} and (b) Current density–voltage characteristics measured under dark conditions for devices with pristine PEDOT:PSS and PEDOT:PSS with 5, 10, 15 and 20 nm a:CuAlO₂ underlayers.

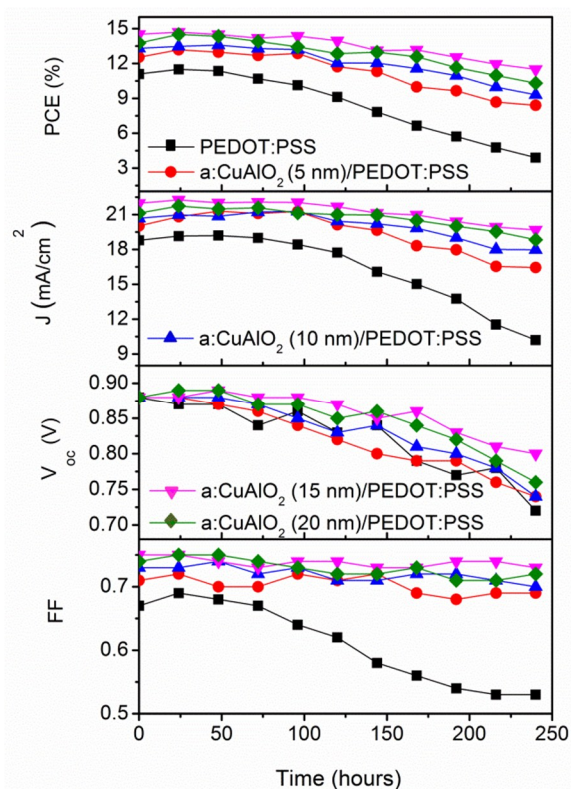


Fig. 9. (a) PCE, (b) J_{sc} , (c) V_{oc} and (d) FF values as a function of ambient storage time of the devices with different configurations of a:CuAlO₂/PEDOT:PSS and pristine PEDOT:PSS hole conductors.

Although PEDOT:PSS is known to yield devices with high performance, its acidic property limits its long term suitability. This is due to the fact that the underlying ITO stands a risk of being eroded after a while by this acidic top layer. This has an adverse effect on the stability of such device. The introduction of an inorganic metal oxide buffer layer which possesses good electrical and optical properties with ambient stability between the PEDOT:PSS and the ITO can therefore not be overemphasised.

This is also advantageous for the perovskite based device as it combines both the excellent electrical properties of PEDOT:PSS and the metal oxide and the ambient stability properties of the metal oxide. To verify this, the stability of CH₃NH₃PbI_{3-x}Cl_x perovskite based devices with various thicknesses of a:CuAlO₂ and devices with pristine PEDOT:PSS was studied. This was done by storing unencapsulated forms of these devices in a dark ambient condition while their parameters are being tested under illumination every 24 hrs over a period of 240 hrs. From Fig. 9, it can be seen that the devices with a:CuAlO₂ show improved stability through the test period with the optimized device retaining about 80 % of its initial PCE whereas the reference device was only able to retain 35 % of its initial PCE as a result of the significant reduction in its J_{sc} and FF. As mentioned above the reduced stability of the reference CH₃NH₃PbI_{3-x}Cl_x perovskite based devices is due to the gradual erosion of the ITO layer as a result of the acidic nature of the PEDOT:PSS top layer.

To investigate the versatility of a:CuAlO₂ in different PSC devices, we extended our investigation to the application of pristine a:CuAlO₂ and a:CuAlO₂/PEDOT:PSS in devices based on CH₃NH₃PbI₃ perovskite prepared by two-step spin-coating method. The application of pristine a:CuAlO₂ is informed by the necessity of developing solar cells which are totally free from the acidic environment created by PEDOT:PSS. The optimized 15 nm a:CuAlO₂ hole extraction layer was adopted for this purpose. The resulting current density–voltage characteristics under AM 1.5 G conditions (100 mWcm⁻²) are shown in Fig. 10(a) and the relevant parameters are summarized in Table 3 (reference cell based on PEDOT:PSS was also fabricated and measured). As expected, due to similarities in energy band alignment, all the devices fabricated exhibited the same V_{oc} (0.88 V). The pristine a:CuAlO₂ (15 nm)-based solar cell exhibits higher J_{sc} (18.58 mA/cm²) than the pristine PEDOT:PSS-based device (16.41 mA/cm²). As previously discussed, this can be ascribed to the higher electrical conductivity exhibited by a:CuAlO₂. However, the FF (0.70) of the pristine PEDOT:PSS-based solar cell is higher than that of the pristine a:CuAlO₂ (0.62). Overall, no significant difference is observed in the PCEs of devices with pristine a:CuAlO₂ and pristine

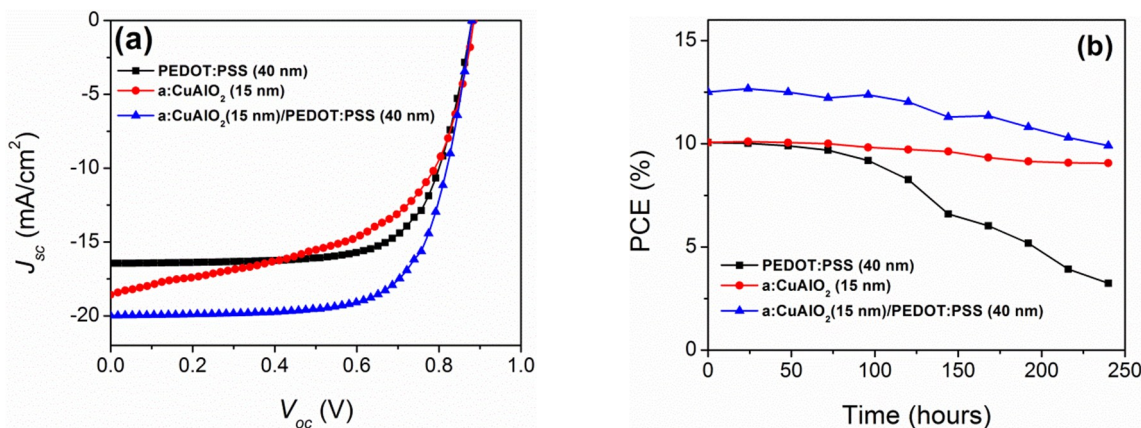


Fig. 10. (a) J - V characteristics and (b) PCE values as a function of ambient storage time of the devices with pristine PEDOT:PSS, pristine a:CuAlO₂ and different configurations of a:CuAlO₂/PEDOT:PSS hole conductors.

Table 3. Photovoltaic parameters of the pristine a:CuAlO₂, pristine PEDOT:PSS and a:CuAlO₂/PEDOT:PSS in CH₃NH₃PbI₃ perovskite based devices.

Hole interfacial layer	J_{sc} (mA/cm ²)	V_{oc} (V)	FF	η (%)
a:CuAlO ₂ (15 nm)	18.58	0.88	0.62	10.14
PEDOT:PSS	16.41	0.88	0.70	10.11
a:CuAlO ₂ (15 nm)/PEDOT:PSS	19.98	0.88	0.71	12.48

PEDOT:PSS. This suggests the suitability of a:CuAlO₂ as an alternative hole selective layer to PEDOT:PSS for perovskite solar cell systems fabricated by the two-step spin-coating method.

Employing a:CuAlO₂/PEDOT:PSS as HTL significantly improves the device performance, with increases in the J_{sc} and FF. As shown in Fig. 10(a). This results in a maximum PCE of 12.48 % which substantially surpasses the performance of pristine a:CuAlO₂ and pristine PEDOT:PSS based devices. As discussed earlier, the enhanced J_{sc} and FF can be interpreted as a consequence of the reduction in series resistance of the device as the a:CuAlO₂ sandwiched between ITO and PEDOT:PSS was able to eliminate the contact resistance created by the harsh acidic effect of PEDOT:PSS on ITO while still retaining its good electrical property. This enables more efficient charge extraction from the perovskite absorber. These results confirm that the sandwiching of a:CuAlO₂ between PEDOT:PSS and ITO is an effective way to improve device performance by reducing series resistance and increasing charge extraction efficiency. The ambient stability of the PCEs of CH₃NH₃PbI₃-based solar cells without encapsulation was characterized and is presented in Fig. 10(b). The pristine a:CuAlO₂-based solar cell shows markedly improved ambient stability as compared to the pristine PEDOT:PSS and a:CuAlO₂/PEDOT:PSS-based devices. The PCE of the pristine a:CuAlO₂-based device remains above 90 % of the initial value even after 240 h of storage in air. In addition, the a:CuAlO₂/PEDOT:PSS-based device retained 80 % of its initial value while the pristine PEDOT:PSS-based device degraded to less than 35 % of its initial PCE. As

mentioned, this lower stability might originate from the acidic characteristics of PEDOT:PSS that erodes the ITO electrode.

Conclusion

In conclusion, we fabricated CH₃NH₃PbI_{3-x}Cl_x perovskite based solar cells with the inverted structure having an a:CuAlO₂/PEDOT:PSS hole conductor bilayer. Due to the significant difference in the thicknesses of the a:CuAlO₂ layer compared to that of the PEDOT:PSS top layer, the PEDOT:PSS top layer presented comparable surface properties with the pristine PEDOT:PSS. This creates a similarity in the growth of the perovskite layer. The decent conductivity of the a:CuAlO₂ in the optimized device and its energy level alignment with PEDOT:PSS yielded an optimized device performance with a PCE of 14.52 % which is significantly higher than that of the reference device (11.10 %). This improvement in device parameters is due to the reduction in charge recombination as a result of enhanced charge separation and collection. On storage for 240 hrs in ambient, the optimized device exhibited better stability as it retained about 80 % of its initial PCE unlike the reference device which was just able to retain only 35 % of its initial PCE. Similar improvement in performance and stability was also observed in devices based on CH₃NH₃PbI₃ prepared by two-step spin-coating method. The improved stability is due to the prevention of the erosion of the ITO layer by the acidic PEDOT:PSS layer as a result of the protective function of the a:CuAlO₂ which is sandwiched between these two layers preventing a direct contact between them. This work presents a feasible

approach to the concurrent improvement of the PCE and stability of inverted PHJ perovskite based solar cells.

Acknowledgements

We acknowledge financial support from the Natural Science Foundation of China (Nos. 61307036 and 61177016), China scholarship council (CSC) and from the Natural Science Foundation of Jiangsu Province (No. BK20130288). This project is also funded by the Collaborative Innovation Center of Suzhou Nano Science and Technology, and by the Priority Academic Program Development of Jiangsu Higher Education Institutions (PAPD).

Supporting Information

Electronic supplementary information (ESI) is available. It includes; experimental section, XRD patterns of a representative a:CuAlO₂ and the pure delafossite crystal phase of the CuAlO₂ ceramic target, typical EDX spectrum confirming Cu:Al:O atomic ratio 1:1:2 for a:CuAlO₂, Arrhenius plots of the PEDOT:PSS film and a:CuAlO₂ with the various film thicknesses showing the variation of logarithmic conductivity as a function of inverse of temperature, tapping mode AFM and plan view SEM images of 5, 10, 15 and 20 nm a:CuAlO₂ films on ITO substrates, tapping mode AFM images of pristine PEDOT:PSS and PEDOT:PSS deposited on 5, 10, 15 and 20 nm a:CuAlO₂ films, Cyclic voltammogram of bare ITO and a:CuAlO₂ in 0.1 M KCl and O 1s XPS core level spectra of various thicknesses of sputtered a:CuAlO₂ on ITO showing varied intensities, the absorption spectra of ITO/PEDOT:PSS/CH₃NH₃PbI_{3-x}Cl_x and ITO/a:CuAlO₂/PEDOT:PSS/CH₃NH₃PbI_{3-x}Cl_x films and table showing the EIS parameters of the perovskite cells with and without a:CuAlO₂.

Notes

*Jiangsu Key Laboratory for Carbon-Based Functional Materials & Devices, Institute of Functional Nano & Soft Materials (FUNSOM), Collaborative Innovation Center of Suzhou Nano Science and Technology, Soochow University, Suzhou, Jiangsu 215123, China.

E-mail: zkwang@suda.edu.cn; lsiao@suda.edu.cn

Notes and references

- N. Ahn, D.-Y. Son, I.-H. Jang, S. M. Kang, M. Chai and N.-G. Park, *J. Am. Chem. Soc.*, 2015, **137**, 8696-8699.
- J.-H. Im, I.-H. Jang, N. Pellet, M. Gratzel and N.-G. Park, *Nat. Nanotechnol.*, 2014, **9**, 927-932.
- Z. Fan, K. Sun and J. Wang, *J. Mater. Chem. A*, Advance Article DOI:10.1039/C5TA04235F.
- C.-G. Wu, C.-H. Chiang, Z.-L. Tseng, M. K. Nazeerudin, A. Hagfeldt and M. Gratzel, *Energy Environ. Sci.*, 2015, **8**, 2725-2733.
- H. Zhou, Q. Chen, G. Li, S. Luo, T.-B. Song, H.-S. Duan, Z. Hang, J. You, Y. Liu and Y. Yang, *Science*, 2014, **345**, 542-546.
- X. Gong, M. Li, X. B. Shi, H. Ma, Z. K. Wang, and L. S. Liao, *Adv. Funct. Mater.* 2015, **25**, 6671-6678.
- J. H. Im, C. R. Lee, J.-W. Lee, S.-W. Park and N.-G. Park, *Nanoscale*, 2011, **3**, 4088-4093.
- G.-C. Xing, N. Mathews, S.Y. Sun, S. S. Lim, Y. M. Lam, M. Gratzel, S. Mhaisalkar and T. C. Sum, *Science*, 2013, **342**, 344-347.
- N. J. Jeon, J. H. Noh, W. S. Yang, Y. C. Kim, S. Ryu, J. Seo and S. I. Seok, *Nature*, 2015, **517**, 476-480.
- C.-H. Chiang, Z.-L. Tseng and C.-G. Wu, *J. Mater. Chem. A*, 2014, **2**, 15897-15904.
- A. Komija, K. Teshima, Y. Shirai and T. Miyasaka, *J. Am. Chem. Soc.*, 2009, **131**, 6050-6051.
- W. S. Yang, J. H. Noh, N. J. Jeon, Y. C. Kim, S. Ryu, J. Seo and S. I. Seok, *Science*, 2015, **348**, 1234-1237.
- Q. Chen, H. Zhou, Z. Hong, S. Luo, H.-S. Duan, H.-H. Wang, Y. Liu, G. Li and Y. Yang, *J. Am. Chem. Soc.*, 2014, **136**, 622-625.
- M. Qian, M. Li, X. B. Shi, H. Ma, Z. K. Wang, and L. S. Liao, *J. Mater. Chem. A* 2015, **3**, 13533-13539.
- M. M. Lee, J. Teuscher, T. Miyasaka, T. N. Murakami and H. J. Snaith, *Science*, 2012, **338**, 643-647.
- N. Li, H. Li, Y. Li, S. Wang and L. Wang, *Phys. Chem. Chem. Phys.*, 2015, Advance Article DOI:10.1039/C503803K.
- A. Abrusci, S. D. Stranks, P. Docampo, H.-L. Yip, A. K.-Y. Jen and H. J. Snaith, *Nano Lett.*, 2013, **13**, 3124-3128.
- J. H. Noh, S. H. Im, J. H. Heo, T. N. Mandal and S. I. Seok, *Nano Lett.*, 2013, **13**, 1764-1769.
- B. Conings, L. Baeten, T. Jacobs, R. Dera, J. D'Haen, J. Manca and H.-G. Boyen, *APL Mater.*, 2014, **2**, 081505.
- T. Leijtens, B. Lauber, G. E. Eperon, S. D. Stranks and H. J. Snaith, *J. Phys. Chem. Lett.*, 2014, **5**, 1096-1102.
- Z. Xiao, Q. Dong, C. Bi, Y. Shao, Y. Yuan and J. Huang, *Adv. Mater.*, 2014, **26**, 6503-6509.
- K. Sun, J. Chang, F. H. Isikgor, P. Li and J. Ouyang, *Nanoscale*, 2015, **7**, 896-900.
- J. You, Z. Hong, Y. (M.) Yang, Q. Chen, M. Cai, T.-B. Song, C.-C. Chen, S. Lu, Y. Liu, H. Zhou and Y. Yang, *ACS Nano*, 2014, **8**, 1674-1680.
- N. Tripathi, M. Yanagida, Y. Shirai, T. Masuda, L. Han and K. Miyano, *J. Mater. Chem. A*, 2015, **3**, 12081-12088.
- J. Qing, H.-T. Chandran, H.-T. Xue, Z.-Q. Guan, T.-L. Liu, S.-W. Tsang, M.-F. Lo and C.-S. Lee, *Org. Electron.*, 2015, **27**, 12-17.
- Q. Xue, Z. Hu, J. Liu, J. Lin, C. Sun, Z. Chen, C. Duan, J. Wang, C. Liao, W. M. Lau, F. Huang, H.-L. Yip and Y. Cao, *J. Mater. Chem. A*, 2014, **2**, 19598-19603.
- Y. Xia, K. Sun, J. Chang and J. Ouyang, *J. Mater. Chem. A*, 2015, **3**, 15897-15904.
- J. H. Kim, P.-W. Liang, S. T. Williams, N. Cho, C.-C. Chueh, M. S. Glaz, D. S. Ginger and A. K.-Y. Jen, *Adv. Mater.*, 2015, **27**, 695-701.
- Z. K. Wang, M. Li, D. X. Yuan, X. B. Shi, H. Ma, L. S. Liao, *ACS Appl. Mater. Interfaces* 2015, **7**, 9645-9651.

- 30 A. S. Subbiah, A. Halder, S. Ghosh, N. Mahuli, G. Hodes and S. K. Sarkar, *J. Phys. Chem. Lett.*, 2014, **5**, 1748-1753.
- 31 J. Y. Jeng, K. C. Chen, T. Y. Chiang, P. Y. Lin, T. D. Tsai, Y. C. Chang, T. F. Guo, P. Chen, T. C. Wen and Y. J. Hsu, *Adv. Mater.*, 2014, **26**, 4107-4113.
- 32 K.-C. Wang, J.-Y. Jeng, P.-S. Shen, Y.-C. Chang, E. W.-G. Diau, C.-H. Tsai, T.-Y. Chao, H.-C. Hsu, P. Y. Lin, P. Chen, T.-F. Guo and T.-C. Wen, *Sci. Rep.*, 2014, **4**, 1-8.
- 33 J. H. Heo, S. H. Im, J. H. Noh, T. N. Mandal, C.-S. Lim, J. A. Chang, Y. H. Lee, H.-J. Kim, A. Sarkar, M. K. Nazeeruddin, M. Gratzel and S. I. Seok, *Nat. Photonics*, 2013, **7**, 486-491.
- 34 Q. Lin, A. Armin, R. C. R. Nagiri, P. L. Burn and P. Meredith, *Nat. Photonics*, 2015, **9**, 106-112.
- 35 L. Hu, W. Wang, H. Liu, J. Peng, H. Cao, G. Shao, Z. Xia, W. Ma and J. Tang, *J. Mater. Chem. A*, 2015, **3**, 515-518.
- 36 Y. Li, J. Zhu, Y. Huang, J. Wei, F. Liu, Z. Shao, L. Hu, S. Chen, S. Yang, J. Tang, J. Yao and S. Dai, *Nanoscale*, 2015, **7**, 9902-9907.
- 37 Z. Wu, S. Bai, J. Xiang, Z. Yuan, Y. Yang, W. Cui, X. Gao, Z. Liu, Y. Jin and B. Sun, *Nanoscale*, 2014, **6**, 10505-10510.
- 38 J. S. Yeo, R. Kang, S. Lee, Y. J. Jeon, N. Myoung, C. L. Lee, D. Y. Kim, J. M. Yun, Y. H. Seo, S. S. Kim and S. I. Na, *Nano Energy*, 2015, **12**, 96-104.
- 39 S.-Y. Lin, C.-M. Wang, K.-S. Kao, Y.-C. Chen and C.-C. Liu, *J. Sol-Gel Sci. Technol.*, 2009, **53**, 51-58.
- 40 F. Xie, W. C. Choy, C. Wang, X. Li, S. Zhang and J. Hou, *Adv. Mater.*, 2013, **25**, 2051-2055.
- 41 S. Murase and Y. Yang, *Adv. Mater.*, 2012, **24**, 2459-2462.
- 42 Y. H. Lou, M. F. Xu, L. Zhang, Z. K. Wang, S. Naka, H. Okada, and L. S. Liao, *Org. Electron.*, 2013, **14**, 2698-2704.
- 43 J. Meyer, R. Khalandovsky, P. Gorn and A. Kahn, *Adv. Mater.*, 2011, **23**, 70-73.
- 44 T. Stubhan, T. Ameri, M. Salinas, J. Krantz, F. Machui, M. Halik and C. J. Brabec, *Appl. Phys. Lett.*, 2011, **98**, 253308-253308.
- 45 M. F. Xu, L. S. Cui, X. Z. Zhu, C. H. Gao, X. B. Shi, Z. M. Jin, Z. K. Wang, and L. S. Liao, *Org. Electron.*, 2013, **14**, 657-664.
- 46 M. F. Xu, X. B. Shi, Z. M. Jin, F. S. Zu, Y. Liu, L. Zhang, Z. K. Wang, and L. S. Liao, *ACS Appl. Mater. Interfaces* 2013, **5**, 10866-10873.
- 47 Y. H. Lou, M. F. Xu, Z. K. Wang, S. Naka, H. Okada, and L. S. Liao, *Appl. Phys. Lett.* 2013, **102**, 113305..
- 48 F. Hou, Z. Su, F. Jin, X. Yan, L. Wang, H. Zhao, J. Zhu, B. Chu and W. Li, *Nanoscale*, 2015, **7**, 9427-9432.
- 49 Y. S. Zou, H. P. Wang, S. L. Zhang, D. Lou, Y. H. Dong, X. F. Song and H. B. Zeng, *RSC Adv.*, 2014, **4**, 41294-41300.
- 50 D. Xiong, X. Zeng, W. Zhang, H. Wang, X. Zhao, W. Chen and Y.-B. Cheng, *Inorg. Chem.*, 2014, **53**, 4106-4116.
- 51 H. Kawazoe, M. Yasukawa, H. Hyodo, M. Kurita, H. Yanagi and H. Hosono, *Nature*, 1997, **389**, 939-942.
- 52 J. Ahmed, C. K. Blakely, J. Prakash, S. R. Bruno, M. Yu, Y. Wu, and V. V. Poltavets, *J. Alloy. Compd.* 2014, **591**, 275-279.
- 53 A. Nattestad, X. Zhang, U. Bach and Y.-B. Cheng, *J. Photon. Energy*, 2011, **1**, 011103.
- 54 J. Bandara and J. P. Yasomancee, *Semicond. Sci. Technol.*, 2007, **22**, 20-24.
- 55 J. Li, X. Wang, S. Shi, X. Song, J. Lv, J. Cui and Z. Sun, *J. Am. Ceram. Soc.*, 2012, **95**, 431-435.
- 56 I. Y. Y. Bu, *Superlattice. Microstruct.*, 2013, **60**, 160-168.
- 57 A. N. Banerjee, S. Kundoo, K. K. Chattopadhyay, *Thin Solid Films*, 2003, **440**, 5-10.
- 58 B. Saha, R. Thapa, S. Jana and K. K. Chattopadhyay, *Indian J. Phys.*, 2010, **84**, 1341-1346.
- 59 K. Sun, Y. Xia, J. Ouyang, *Sol. Energy Mater. Sol. Cells*, 2012, **97**, 89-96.
- 60 A. M. Nardes, M. Kemerink, M. M. de Kok, E. Vinken, K. Maturova, R. A. J. Jassen, *Org. Electron.*, 2008, **9**, 727-734.
- 61 W. G. Zeier, S. Zhou, B. Lopez-Bermudez, K. Page and B. C. Melot, *ACS Appl. Mater. Interfaces*, 2014, **6**, 10900-10907.
- 62 R.-J. Chen, M. Huang, W.-Z. Huang, Y. Shen, Y.-H. Lin and C.-W. Nan, *J. Mater. Chem. A*, 2014, **2**, 13277-13282.
- 63 M. Chelvayohan and C. H. B. Mee, *J. Phys. C: Solid State Phys.*, 1982, **15**, 2305-2312.
- 64 W. Li and D. Y. Li, *J. Chem. Phys.*, 2005, **122**, 064708.
- 65 R. Ozawa, K. Kaykham, A. Hiraishi, Y. Suzuki, N. Mori, T. Yaguchi, J. Itoh and S. Yamamoto, *Appl. Surf. Sci.*, 1999, **146**, 162-168.
- 66 J. S. Kim, F. Cacialli and M. Granstrom, *Synthetic Met.*, 1999, **101**, 111-112.
- 67 T. A. Beierlein, W. Brutting, H. Riel, E. K. Haskal and W. Rieβ, *Synthetic Met.* 2000, **111-112**, 295-297.
- 68 M. T. Greiner, M. G. Helander, Z. -B. Wang, W. -M. Tang and Z. -H. Lu, *J. Phys. Chem. C*, 2010 **114**, 19777-19781.
- 69 S. Noh, C. K. Suman, D. Lee, S. Kim and C. Lee, *J. Nanosci. Nanotechnol.*, 2010, **10**, 6815-6818.
- 70 J. Huang, L. Chen, F. He, T. Zhang, G. Niu, J. Pan, Z. Xiong and Q. Song, *J. Phys D: Appl. Phys.*, 2012, **45**, 195101.
- 71 S. Chang, H. Park, J. J. Cheng, P. H. Rekemeyer and S. Gradecak, *J. Phys. D: Appl. Phys.*, 2004, **47**, 394016.
- 72 J. Kim, G. Kim, T. K. Kim, S. Kwon, H. Back, J. Lee, S. H. Lee, H. Kang and K. Lee, *J. Mater. Chem. A*, 2014, **2**, 17291-17296.

Graphical abstract

